

Evidence for a sub-Jovian planet in the young TWA 7 disk

<https://doi.org/10.1038/s41586-025-09150-4>

Received: 25 July 2024

Accepted: 13 May 2025

Published online: 25 June 2025

Open access

 Check for updates

A.-M. Lagrange^{1,2}✉, C. Wilkinson¹, M. Mâlin^{3,4}, A. Boccaletti¹, C. Perrot¹, L. Matrà⁵, F. Combes⁶, H. Beust², D. Rouan¹, A. Chomez^{1,2}, J. Milli², B. Charnay¹, S. Mazevet⁷, O. Flasseur⁸, J. Olofsson⁹, A. Bayo⁹, Q. Kral¹, A. Carter⁴, K. A. Croots⁴, P. Delorme², G. Chauvin⁷, P. Thebault¹, P. Rubini¹⁰, F. Kiefer¹, A. Radcliffe¹, J. Mazoyer¹, T. Bodrito¹¹, S. Stasevic¹ & M. Langlois⁹

Planets are thought to form from dust and gas in protoplanetary disks, with debris disks being the remnants of planet formation. Aged a few million up to a few billion years, debris disks have lost their primordial gas, and their dust is produced by steady-state collisions between larger, rocky bodies^{1,2}. Tens of debris disks, with sizes of tens, sometimes hundreds, of astronomical units have been resolved with high-spatial-resolution, high-contrast imagers at optical and near-infrared or (sub) millimetre interferometers^{3,4}. They commonly show cavities, ring-like structures and gaps, which are often regarded as indirect signatures of the presence of planets that gravitationally interact with unseen planetesimals^{2,5}. However, no planet responsible for these features has been detected yet, probably because of the limited sensitivity (typically $2\text{--}10 M_J$) of high-contrast imaging instruments (see, for example, refs. 6–9) before the James Webb Space Telescope. Here we have used the unprecedented sensitivity of the James Webb Space Telescope's Mid-Infrared Instrument^{10,11} in the thermal infrared to search for such planets in the disk of the approximately 6.4-Myr-old star TWA 7. With its pole-on orientation, this three-ring debris disk is indeed ideally suited for such a detection. We unambiguously detected a source 1.5 arcsec from the star, which is best interpreted as a cold, sub-Jupiter-mass planet. Its estimated mass (about $0.3 M_J$) and position (about 52 AU, de-projected) can thoroughly account for the main disk structures.

The disk around TWA 7 is one of the youngest (6.4 ± 1 Myr old; ref. 12), debris disks known to date. TWA 7 is a close (about 34 pc; ref. 13), low-mass ($0.46 M_\odot$; ref. 14) member of the young TW Hydra association, sometimes classified as a weak-line, non-accreting T-Tauri star¹⁵. The disk, resolved by the Near Infrared Camera and Multi-Object Spectrometer (NICMOS) on the Hubble Space Telescope (HST)¹⁶, is one of the rare ones resolved around M stars. It is seen almost pole-on^{17,18}, a most favourable configuration to precisely estimate its radial distribution and to look for planets. The most recent modelling of the disk surface density deduced from polarimetric data from the Spectro-Polarimetric High Contrast Imager for Exoplanets Research (SPHERE) on the Very Large Telescope (VLT)¹⁸ includes a ring peaking at 28 AU and extending out to more than 100 AU (R1), a narrow (less than 7 AU full-width at half-maximum) ring at 52 AU (R2) and a broader (more than 40 AU full-width at half-maximum) structure (93 AU; R3; Figs. 1 and 4 from ref. 18). No planet has been detected so far, with detection limits roughly estimated to $0.5\text{--}1 M_J$ beyond 50 AU (Extended Data Fig. 6 and Supplementary Information).

The coronagraphic images of TWA 7 taken with the F1140C filter (central wavelength = $11.3 \mu\text{m}$, bandwidth = $0.8 \mu\text{m}$) of the Mid-Infrared

Instrument (MIRI) on the James Webb Space Telescope (JWST)¹⁹ were obtained on 21 June 2024 during cycle 2 (ID 3662; principal investigator, A.-M.L.; Extended Data Table 1). The details on the data reduction procedure are described in the Methods. The main critical step is the subtraction of the residual diffracted light leaking from the MIRI coronagraph using a reference star observed with the same set-up. This process is necessary to bring the contrast ratio with respect to the star to a level of $10^{-5}\text{--}10^{-4}$ beyond angular separations of about 0.5 arcsec. The final image, presented in Fig. 1, reveals three sources within 10 arcsec from TWA 7, the properties of which are listed in Extended Data Table 2. One source at about 4.7 arcsec from TWA 7 (position angle 107°) was classified as a stellar background source, already detected in ancillary optical data from the Space Telescope Imaging Spectrograph (STIS) on the HST as well as near-infrared data from the NICMOS on the HST and the SPHERE on the VLT. The second one, located about 6.7 arcsec east of TWA 7, and spatially resolved, has no counterpart in the data from the SPHERE on the VLT, or in the data from the NICMOS or the STIS on the HST (taking into account TWA 7 proper motion ($-118.751 \pm 0.023 \text{ mas yr}^{-1}$, $-19.648 \pm 0.026 \text{ mas yr}^{-1}$; ref. 20)). Its location in the MIRI image is consistent with that of a bright source

¹LIRA, Observatoire de Paris, Université PSL, Sorbonne Université, Université Paris Cité, CY Cergy Paris Université, CNRS, Meudon, France. ²Université Grenoble Alpes, CNRS, IPAG, Grenoble, France. ³Department of Physics & Astronomy, Johns Hopkins University, Baltimore, MD, USA. ⁴Space Telescope Science Institute, Baltimore, MD, USA. ⁵School of Physics, Trinity College Dublin, University of Dublin, Dublin, Ireland. ⁶Observatoire de Paris, LUX, PSL University, Collège de France, Sorbonne University, CNRS, Paris, France. ⁷Observatoire de la Côte d'Azur, Université Côte d'Azur, Nice, France. ⁸Centre de Recherche Astrophysique de Lyon, Université Claude Bernard Lyon 1, CNRS, ENS, Saint-Genis-Laval, France. ⁹European Southern Observatory, Garching bei Muenchen, Germany. ¹⁰Pixyl, La Tronche, France. ¹¹Département d'Informatique de l'École Normale Supérieure (ENS-PSL, CNRS, Inria), Paris, France. [✉]e-mail: anne-marie.lagrange@obspm.fr

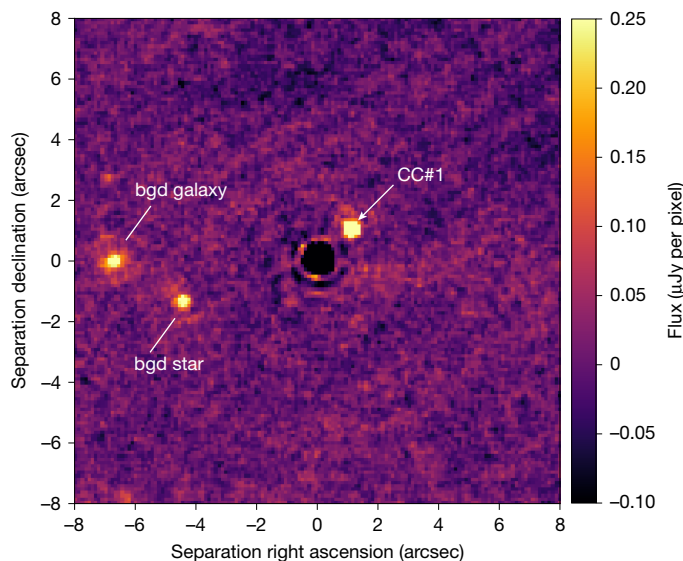


Fig. 1 | JWST MIRI image of TWA 7 in the F1140C filter. North is up, and east is left. The status of three identified sources is indicated. Note that the faint signal north of the background galaxy is an artefact. bgd, background.

in Atacama Large Millimeter Array (ALMA) band 7 (346 GHz) data from 2016 (ref. 21), given the proper motion of the TWA 7 system between the ALMA and MIRI observations. This object therefore has the characteristics of a highly reddened background source. It is reminiscent of the JWST observations of the HR 8799 multi-planetary system, for which a $z \approx 1$ galaxy was detected in the MIRI data taken at both 10 and 15 μm , and in ALMA band 7 data as well, but never identified in the near-infrared²². The third source, located about 1.5 arcsec northwest of TWA 7 (about 51 AU, projected separation) is unique to these MIRI observations. Hence, this source (hereafter, CC#1) is extremely red, and is not compatible with any background or foreground star.

No data are available to test whether this third source shares a common proper motion with the star. In this context, in the following, we discuss the possible nature of this object. The first origin that one can consider is a Solar System object. Yet, most Solar System objects have proper motion between 5 and 40 arcsec h^{-1} (ref. 23). Even very remote, low-proper-motion small Solar System objects such as the dwarf planets Eris (semi-major axis of about 68 AU) and Sedna (semi-major axis of about 510 AU) showed proper motion of 1.4 arcsec h^{-1} (ref. 24) and 1.7 arcsec h^{-1} (ref. 25), respectively, at the time of their discovery. No trail was observed during the 2-h-long exposures, and no apparent motion was observed between the two images recorded during the sequences taken 2 h apart, indicating that CC#1 has a proper motion of less of than about 0.05 arcsec h^{-1} . A Solar System object with such a low proper motion would be located at more than 200 AU. For such a cold object, reflected light would dominate in the MIRI F1140C filter and would require a Neptune-like size to fit the flux measured for CC#1 (for a geometric albedo of 0.1–0.3). It was checked whether such a scenario could be compatible with the hypothetical Planet Nine²⁶. On the basis of the constraints from the planetary ephemeris²⁷ and the predictions of the orbit of Planet Nine²⁸, a Solar System origin for CC#1 can definitely be excluded.

The second possible origin is a background galaxy. Like the background galaxy seen east of TWA 7, CC#1 has no reported counterpart at optical and near-infrared wavelengths. However, in contrast to this galaxy, it has no detected counterpart in the ALMA band 7 data (see details in Supplementary Information). The detection of this unresolved source at 11.3 μm , its non-detection in ALMA band 7 and the measured upper limits at 1.6 μm in the data from the SPHERE on VLT (Supplementary Information) could still be compatible with intermediate-redshift

star-forming galaxies. Using such galaxy templates at various redshifts and published galaxy counts in JWST fields of view, we estimated that the probability of finding one such galaxy in a region of 1.5 arcsec radius centred on TWA 7 is about 0.34% (Methods). This probability is low, albeit non-zero. The location of the source with respect to the disk structure, right in a circumstellar ring gap (see below), makes the galaxy hypothesis even more unlikely.

The third and last possible origin is a planet. A forward modelling approach is used to constrain the properties of this planet. Using the HADES model²⁹, it is possible to find fits for the JWST photometric data point while accounting for the 5σ upper limits provided by the high-contrast images at 1.59 μm (H2) and 1.67 μm (H3) from the SPHERE on the VLT (Fig. 2). HADES considers the thermal evolution of the planet; it assumes that the planet and the stars are coeval. Atmospheric fits incorporating water clouds indicate a narrow range, regardless of other parameters, for the effective temperature between 305 and 335 K (Extended Data Fig. 3 and Extended Data Table 3), and a mass of about $0.3 M_J$. A metallicity range above solar is required. Additional data will be necessary to further constrain this parameter.

As a comparison and extra mass estimation, evolutionary models of cold, low-mass planets³⁰ combined with our estimation of effective temperature are used; they lead to a comparable mass of close to $0.3 M_J$ (Extended Data Fig. 4) for metallicities less than 2.5, as available in their framework. These two consistent results indicate that the planet mass is substantially below $1 M_J$. The current best estimate is around $0.3 M_J$, and is only weakly dependent on the underlying details of the two models used. It, however, depends on the age of the planet, assumed here to be coeval with its parent star. A younger planet would lead to a smaller mass.

The observed source is located right on the R2 narrow ring, and, moreover, within a region identified by ref. 18 as underdense compared to the rest of the ring (Fig. 3a). This is very reminiscent of simulations of resonant rings predicted by early works^{31,32} for closer and less massive planets, which led to the proposal of such a possible situation for the TWA 7 system¹⁸.

Dedicated N -body simulations were conducted for a planet with a mass of $0.34 M_J$, located at 52 AU around the $0.46 M_\odot$ central star. This value is consistent with the measured projected separation, assuming that the planet and the $\approx 13^\circ$ -inclined disk are coplanar. The simulation also included a disk of 200,000 planetesimals, distributed between 20 and 130 AU. These parameters were selected to roughly match the boundaries of the observed disk. The planetesimal disk was assumed to be coplanar with the planet's orbit, with an initial surface density proportional to $1/r$. The eccentricities of the planetesimals were chosen to range between 0 and 0.01, and the planet was assumed to evolve on a circular orbit. The simulations, which spanned 10 Myr, were performed using the symplectic N -body code swift_rmv3 (ref. 33), which provides a first-order treatment of close encounters.

A top view of the resulting distribution of planetesimals after 6 Myr is shown in Fig. 3b. Planetary perturbations efficiently carve the disk over about 30 AU, but leave a narrow ring at 52 AU, as well as a relative void (underdense) around the planet. The latter structure is characteristic of a ring of co-orbital planetesimals with the planets, trapped in a 1:1 resonance with it. The similarity between the TWA 7 disk image and the simulation (Fig. 3a,b) is remarkable. In this context, the observed R2 ring would correspond to the ring of co-orbiters with the planet. We nevertheless expect some differences between both distributions owing to the radiation pressure acting on the grains. Additional information on the grain size distribution is needed to compute the effects of radiation pressure and refine the dynamical modelling.

The low likelihood of a background galaxy, the successful fit of the MIRI flux and SPHERE upper limits by a $0.3 M_J$ planet spectrum and the fact that an approximately $0.3 M_J$ planet at the observed position would naturally explain the structure of the R2 ring, its underdensity at the

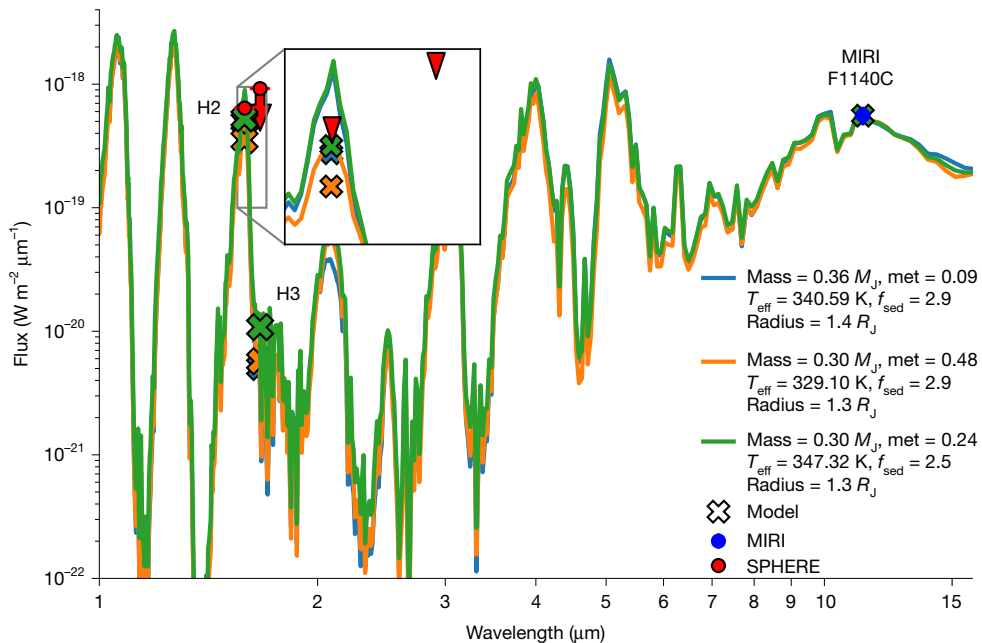


Fig. 2 | Fitting of the candidate companion's available data using the HADES model. Modelled photometry is shown with crosses. The 1–15- μm spectra correspond to representative solutions that fit the observed flux of TWA 7b in the JWST F1140C filter (blue), with respect to the 5σ upper limits from the VLT SPHERE data in the H2 and H3 filters (red), and are consistent with an age

6.4 ± 1 Myr. The bandwidths of H2 and H3 are $0.052 \mu\text{m}$ and $0.054 \mu\text{m}$, respectively. A zoomed-in view around H2 and H3 highlights their bandwidths and the integrated model spectrum points below the upper limit. met, metallicity; T_{eff} , effective temperature; f_{sed} , sedimentation rate.

planet's position and the gaps provide compelling evidence supporting a planetary origin for the observed source. Like the planet β Pictoris b, which is responsible for an inner warp in a well-resolved—from optical to millimetre wavelengths—debris disk³⁴, TWA 7b is very well suited for further detailed dynamical modelling of disk–planet interactions. To do so, deep disk images at short and millimetre wavelengths are needed to constrain the disk properties (grain sizes and so on). Refining the planet mass determination can be carried out with additional JWST photometry and possibly spectroscopy. Measuring the orbital parameters (eccentricity, in particular) is more challenging given the

long orbital period (about 550 yr) of the planet. Yet, one notes that a planet on an eccentric orbit would rapidly destroy R2.

As it is angularly well resolved from the star, TWA 7b is suited for direct spectroscopic investigations, providing the opportunity to study the interior and the atmosphere of a non-irradiated sub-Jupiter-mass, cold (about 320 K) exoplanet, and start comparative studies with our much older and cooler Solar System giants, as well as with the recently imaged cold (about 275 K) but more massive ($6 M_J$) planet eps Ind Ab ³⁵. Improved estimations of its metallicity and temperature will further constrain its mass.

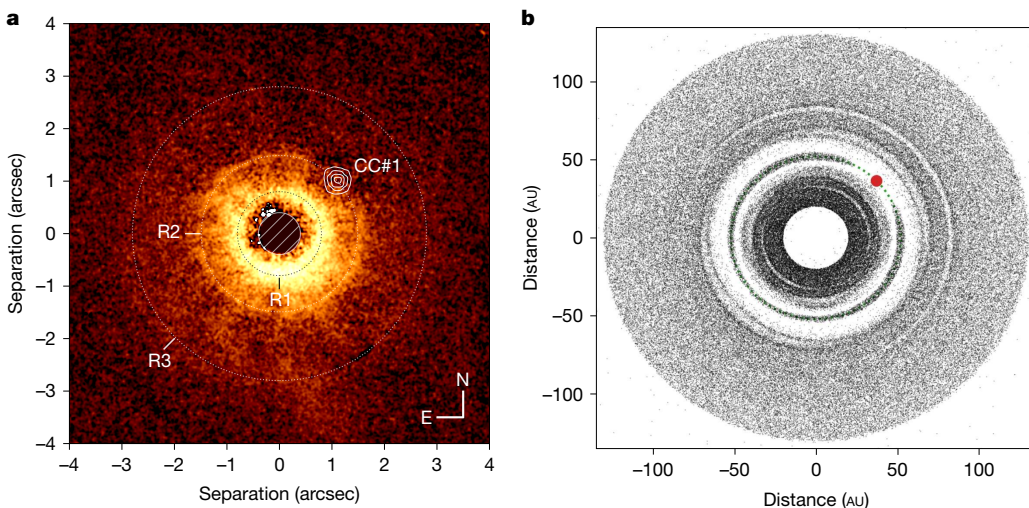


Fig. 3 | Image of the TWA disk and candidate companion and simulations. **a**, Polarimetric image (in log scale) of the disk composed of the sum of three epochs (26 April 2016 presented in ref. 17, 20 March 2017 presented in ref. 18, and a new epoch, 8 February 2022, reduced as in ref. 18) from the SPHERE Infrared Dual-Band Imager and Spectrograph (IRDIS), with the MIRI image (resampled to the SPHERE pixel size) as an overlay with contours. The log of

these data is provided in Supplementary Table 2. The peak densities of the rings are also indicated. The central hatched disk is a numerical mask to hide the stellar residuals. **b**, Disk simulations. Top view of a disk of massless planetesimals perturbed by a $0.34-M_J$ planet at 52 AU, on a circular orbit, after 6 Myr (see details in text). The orbit of the perturbing planet is sketched in green and the location of the planet on its orbit is shown in red.

The present results show that the JWST MIRI has opened up a new window in the study of sub-Jupiter-mass planets using direct imaging. Indeed, TWA 7b (about $100 M_{\oplus}$) is at least ten times lighter than the exoplanets directly imaged so far, and planets as light as $25\text{--}30 M_{\oplus}$ could have been detected if present at 1.5 arcsec from the star or beyond.

Online content

Any methods, additional references, Nature Portfolio reporting summaries, source data, extended data, supplementary information, acknowledgements, peer review information; details of author contributions and competing interests; and statements of data and code availability are available at <https://doi.org/10.1038/s41586-025-09150-4>.

1. Backman, D. E. & Paresce, F. in *Protostars and Planets IV* 639 (1993).
2. Wyatt, M. C. Evolution of debris disks. *Annu. Rev. Astron. Astrophys.* **46**, 339–383 (2008).
3. Matrà, L. et al. REsolved ALMA and SMA Observations of Nearby Stars (REASONS): A population of 74 resolved planetesimal belts at millimetre wavelengths. *Astron. Astrophys.* **693**, A151 (2025).
4. Pawellek, N. & Krivov, A. *Resolved Debris Discs* (Astrophysikalisches Institut und Universitäts-Sternwarte); <https://www.astro.uni-jena.de/index.php/theory/catalog-of-resolved-debris-disks.html>.
5. Shannon, A. et al. The unseen planets of double belt debris disc systems. *Mon. Not. R. Astron. Soc.* **462**, L116–L120 (2016).
6. Su, K. Y. L. et al. Asteroid belts in debris disk twins: Vega and Fomalhaut. *Astrophys. J.* **763**, 118 (2013).
7. Milli, J. et al. Near-infrared scattered light properties of the HR 4796 A dust ring. A measured scattering phase. *Astron. Astrophys.* **599**, A108 (2017).
8. Pearce, T. et al. Planet populations inferred from debris discs. Insights from 178 debris systems in the ISPY, LEECH, and LISTEN planet-hunting surveys. *Astron. Astrophys.* **659**, A135 (2022).
9. Faramaz, V. et al. A detailed characterization of HR 8799's debris disk with ALMA in band 7. *Astron. J.* **161**, 271 (2021).
10. Gardner, J. P. et al. The James Webb Space Telescope Mission. *Publ. Astron. Soc. Pac.* **135**, 068001 (2023).
11. Wright, et al. The Mid-Infrared Instrument for the James Webb Space Telescope, II: design and build. *Publ. Astron. Soc. Pac.* **125**, 595 (2015).
12. Binks, A. S. et al. A kinematically hot population of young stars in the solar neighbourhood. *Mon. Not. R. Astron. Soc.* **494**, 2429–2439 (2020).
13. Gaia Collaboration et al. Gaia data release 3. Summary of the content and survey properties. *Astron. Astrophys.* **674**, A1 (2023).
14. Stassun, K. G. et al. The TESS input catalog and candidate target list. *Astron. J.* **156**, 102 (2018).
15. Nicholson, B. A. et al. The surface magnetic activity of the weak-line T Tauri stars TWA 7 and TWA 25. *Mon. Not. R. Astron. Soc.* **504**, 2461–2473 (2021).
16. Choquet, E. et al. First images of debris disks around TWA 7, TWA 25, HD 35650, and HD 377. *Astrophys. J.* **817**, L2 (2016).
17. Olofsson, J. et al. Resolving faint structures in the debris disk around TWA 7. Tentative detections of an outer belt, a spiral arm, and a dusty cloud. *Astron. Astrophys.* **617**, A109 (2018).
18. Ren, B. et al. A layered debris disk around M Star TWA 7 in scattered light. *Astrophys. J.* **914**, 95 (2021).
19. Rieke, et al. The Mid-Infrared Instrument for the James Webb Space Telescope, VII: the MIRI detectors. *Publ. Astron. Soc. Pac.* **127**, 665 (2015).
20. VizieR Online Data Catalog: Gaia EDR3 (Gaia Collaboration, 2020).
21. Bayo, A. et al. Sub-millimetre non-contaminated detection of the disc around TWA 7 by ALMA. *Mon. Not. R. Astron. Soc.* **486**, 5552–5557 (2019).
22. Boccaletti, A. et al. Imaging detection of the inner dust belt and the four exoplanets in the HR 8799 system with JWST's MIRI coronagraph. *Astron. Astrophys.* **686**, A33 (2024).
23. Mahlke, M. et al. Mining the Kilo-Degree Survey for solar system objects. *Astron. Astrophys.* **610**, A21 (2018).
24. Brown, M. E. et al. Discovery of a planetary-sized object in the Scattered Kuiper Belt. *Astrophys. J.* **635**, L97–L100 (2005).
25. Brown, M. E. et al. Discovery of a candidate inner Oort Cloud planetoid. *Astrophys. J.* **617**, 645 (2004).
26. Batygin, K. et al. Evidence for a distant giant planet in the Solar System. *Astron. J.* **151**, 22 (2016).
27. Fienga, A. et al. New constraints on the location of P9 obtained with the INPOP19a planetary ephemeris. *Astron. Astrophys.* **640**, A6 (2020).
28. Brown, M. E. & Batygin, K. The orbit of Planet Nine. *Astron. J.* **162**, 219 (2021).
29. Wilkinson, C. Breaking degeneracies in exoplanetary parameters through self-consistent atmosphere–interior modelling. *Astron. Astrophys.* **692**, A113 (2024).
30. Linder, E. et al. Evolutionary models of cold and low-mass planets: cooling curves, magnitudes, and detectability. *Astron. Astrophys.* **623**, A85 (2019).
31. Ozernoy, L. M. et al. Signatures of extrasolar planets in dust debris disks. *Astrophys. J.* **537**, L147 (2000).
32. Stark, C. C. & Kuchner, M. J. The detectability of exo-Earths and super-Earths via resonant signatures in exozodiacal clouds. *Astrophys. J.* **686**, 637 (2008).
33. Levison, H. F. & Duncan, M. J. The long-term dynamical behavior of short-period comets. *Icarus* **108**, L18 (1994).
34. Lagrange, A.-M. et al. A giant planet imaged in the disk of the young star beta Pictoris. *Science* **329**, 57–59 (2010).
35. Matthews, E. C. et al. A temperate super-Jupiter imaged with JWST in the mid-infrared. *Nature* **633**, 789–792 (2024).

Publisher's note Springer Nature remains neutral with regard to jurisdictional claims in published maps and institutional affiliations.



Open Access This article is licensed under a Creative Commons Attribution-NonCommercial-NoDerivatives 4.0 International License, which permits any non-commercial use, sharing, distribution and reproduction in any medium or format, as long as you give appropriate credit to the original author(s) and the source, provide a link to the Creative Commons licence, and indicate if you modified the licensed material. You do not have permission under this licence to share adapted material derived from this article or parts of it. The images or other third party material in this article are included in the article's Creative Commons licence, unless indicated otherwise in a credit line to the material. If material is not included in the article's Creative Commons licence and your intended use is not permitted by statutory regulation or exceeds the permitted use, you will need to obtain permission directly from the copyright holder. To view a copy of this licence, visit <http://creativecommons.org/licenses/by-nc-nd/4.0/>.

© The Author(s) 2025

Methods

JWST observations and data reduction and analysis

Data. Coronagraphic observations were performed with the 4QPM_1140 coronagraph paired with the F1140C filter. The details of the observations are given in Extended Data Table 1. We obtained two roll angles (difference of 7.835°) to mitigate the attenuation of the coronagraph in the field of view, in case an object falls close to one phase transition of the 4QPM. Each coronagraphic observation was 2 h long, hence a total of 4 h on the science target. Background observations were observed immediately after the science exposures in a two-point dithering mode, for a total of 4 h.

A reference star, CD-23-9765, was observed back-to-back with the target in the same configuration with the aim to subtract the starlight diffraction after the coronagraph. The reference shares similar brightness and spectral type with the target, and is angularly close. It was observed with nine-point small-grid dithering (SGD) to apply post-processing algorithms such as principal component analysis (PCA)³⁶. In total, the reference star was observed for about 1 h and comes with dedicated background observations.

Using comparison with simulated coronagraphic images, as in ref. 37, we were able to estimate a pointing accuracy on the 4QPM of about 2 mas per axis, significantly lower than the 10-mas step of the SGD. We also confirmed the detector coordinates of the 4QPM_1140 mask (119.758, 112.158 as provided in the JWST Calibration Reference Data System).

Data analysis. The data reduction follows the steps described in refs. 21,38. Level 1 data are retrieved from the Mikulski Archive for Space Telescopes (MAST), processed with v1.14.0 of the pipeline together with Calibration Reference Data System file 1241. Images are registered to the coronagraph centre. Calibrated files ('cal' files) are produced in-house with the JWST pipeline for each roll, by subtracting the background and converting the photometric units (data numbers per second to mega-janskys per steradian). The background is built from the minimum per pixel of the two dithers. We skipped the flat-field correction, which is not appropriate for the MIRI coronagraph²².

We took advantage of the diversity brought by the SGD mode to build a reference frame to subtract the stellar diffraction. We tested various algorithms and retained a linear combination (which uses the downhill simplex minimization) of the nine SGD reference star images, as well as the PCA, as the two algorithms providing the best detection of CC#1. To mitigate the over-subtraction effect, a numerical masking is implemented to ignore some parts of the image. We obtained the best compromise by selecting the annular region between 0.5 arcsec and 3 arcsec, and the three sources were masked with a $1\lambda/D$ patch, with λ representing the observing wavelength and D the telescope diameter (we checked that the CC#1 flux measurements are similar with a different region: 2–3 arcsec). We proceeded similarly for the PCA, using eight components to build the final image that is subtracted to the data, in an annular region from 0.5 arcsec to 5 arcsec (point sources not masked). Despite the bad-pixel correction applied on the raw coronagraphic images, the subtracted images with the reference star are still affected by a few bad pixels, both with the linear combination and PCA. We further apply a σ -clipping function to correct for these remaining bad pixels. Finally, the images are rotated to align north up, considering the aperture position angles: 121.45° for roll 1 and 129.27° for roll 2, as well as the V3 axis orientation on the detector (4.835°).

Next, extracting the flux and position of the CC#1 requires modelling its point spread function (PSF), which can vary spatially and nonlinearly owing to the attenuation of the coronagraph for which the phase transitions extend across the whole field of view. We used both the diffraction code developed in refs. 39,40 and WebbPSF⁴¹ to simulate the MIRI PSF, taking into account the coronagraph, considering the configuration of mask, stop and filter ('FQPM1140', 'MASKFQPM' and 'F1140C', according

to the WebbPSF terminology). The position of CC#1 is approximated with a Gaussian fit, passing the sky coordinates to the former diffraction code and detector coordinates to WebbPSF to calculate the PSF of CC#1 accounting for the coronagraph attenuation. We measured the coronagraph transmission with both PSF estimates. The flux of the PSF model at the position of CC#1 is integrated in a $1.5\lambda/D$ aperture (to match the aperture used for photometric measurements), and compared to that at 10 arcsec (far away from the coronagraph influence). The two approaches give similar transmissions: 0.66 and 0.62 in roll 1 and 0.31 and 0.28 in roll 2. Therefore, CC#1 is significantly closer to one 4QPM transition in roll 2 than in roll 1, so both its astrometry and photometry can be affected (Extended Data Fig. 1). We measured a signal-to-noise ratio of 30 and 18, respectively, for roll 1 and roll 2, using the linear combination method. In the roll 2 image, the PSF is more asymmetrical as the planet is closer to the quadrant edge in comparison to roll 1, so we decided to consider only roll 1 data for the photometric analysis.

On the basis of these CC#1 PSF models, we extracted the flux and the photometry of the object by minimizing the residuals between the reduced JWST data and a PSF model in a $1.5\lambda/D$ area with three free parameters (positions and flux) and using either a downhill simplex algorithm or the Nelder–Mead algorithm⁴². For comparison, we also used aperture photometry, but this required implementation of an aperture correction based on simulated PSF (ratio of the total flux in the PSF to the flux integrated in the $1.5\lambda/D$ aperture).

The flux extraction is applied both on the photometrically calibrated files (.cal), which directly provides CC#1 flux in mega-janskys per steradian, and on the uncalibrated files (.rate), which requires to measure a contrast with respect to the non-coronagraphic image of the star. As detailed previously²², the contrast measurement relies on commissioning data either on target acquisition images that come with the telescope pointing procedure but are obtained with a neutral density filter, or from images obtained on and off the coronagraph on another star. The method using target acquisition shows some net discrepancies, probably because the target acquisition filter is very broad (about 8–18 μm) and the targets have different spectral types (M3 for TWA 7 and K0 or K5 for the commissioning targets). Besides, the emission of the TWA 7 disk is expected to become significant beyond 15 μm . As a result, we did not use the target acquisition method in the following. The final photometric values are based on the linear combination and PCA technique to suppress the starlight. We averaged the values of the different methods (calibrated files and contrast, aperture and PSF model for the photometric extraction) and the error bar is built from the extreme values ((max – min)/2) for being conservative. We measured a flux density of $5.60 \pm 0.97 \times 10^{-19} \text{ W m}^{-2} \mu\text{m}^{-1}$ for CC#1. The fluxes of the other sources are given in Extended Data Table 2. Note that we also tested the typical 'injection–recovery' method directly in the raw data, but did not notice any significant differences for the extracted flux of the planet.

Estimation of the probability for an intermediate-redshift star-forming galaxy

To estimate the probability that the source labelled CC#1 is a galaxy, we have taken into account the three constraints on the fluxes or upper limits at 1.6, 11 and 870 μm . The source has a flux of 22 μJy at 11 μm , and is not detected with ALMA at 870 μm , but with a tapered resolution of 2 arcsec. The measured 3σ upper limit for an unresolved source at the position of the MIRI source is 96 μJy (ref. 21). Combining all ALMA observations (see Extended Data Fig. 5), the 3σ upper limit is 76 μJy , in a beam of $0.29 \text{ arcsec} \times 0.24 \text{ arcsec}$ (see a detailed analysis and estimation in the Supplementary Information). The third constraint is from the non-detection at 1.6 μm with VLT SPHERE, with an upper limit of approximately 0.6 μJy for a point source (about 60 mas in size). However, we have to take into account the fact that a low- z galaxy could be extended in the calculation of its maximum flux at 2 μm . Indeed, the size of a galaxy is expected to vary from one wavelength to the other: at 1.6 μm ,

Article

the disk of old stars dominates, so the source is more extended, of the order of 10 kpc, whereas at 11 μ m and 870 μ m, the nuclear star-forming region dominates, and will appear more concentrated, of the order of 100–500 pc. We therefore considered the flux limit of an extended (0.6 arcsec) source in the SPHERE data (that is, 60 μ Jy).

Two types of galaxy might comply with these three constraints: star-forming galaxies or active nucleus (AGN) or a combination of both, with a redshift between $z = 0.1$ and 1. For such galaxies, at lower redshifts, where 1 arcsec is smaller than 2 kpc, the source would probably look extended (up to 5 arcsec) for wavelengths between 1 and 4 μ m (ref. 43). At higher redshifts, the peak of the emission usually located at 100 μ m will enter the ALMA domain at about 1 mm, and it should have been detected by ALMA⁴⁴.

As the density of the cosmic star formation rate increases considerably with redshift between $z = 0$ and 1, starbursts at $z = 0$ are good templates for star-forming galaxies at $z = 0.1$ to 1. The starburst is in general nuclear. It can be highly peaked in the centre, or distributed in a ring of about 100- μ m radius (like in M82), but the emitting size at 100- μ m rest frame will be no more than typically 1 kpc. This corresponds to an angular size of about 0.55 arcsec at $z = 0.1$, about 0.16 arcsec at $z = 0.5$, and about 0.12 arcsec at $z = 1$. We also considered AGN templates. The nucleus is then a point source at long wavelengths, while the galaxy host is extended (about 10 kpc) at the shortest wavelengths.

The probability to find a $z = 0.1$ to 1 star-forming galaxy with a flux at 11 μ m of $22 \pm 3.8 \mu$ Jy (hence, within a range of 7.6 μ Jy) in a field of view of 10×10 arcsec can be estimated readily through the source counts, from refs. 45–48. A probability of 50% is found in the redshift range $z = 0.1$ to 1.

To take into account the other constraints at 1.6 and 870 μ m, we used the Spitzer Wide-Area Infrared Extragalactic Survey (SWIRE) templates, from ref. 49, http://www.iasf-milano.inaf.it/~polletta/templates/swire_templates.html which include 14 templates of starbursts and AGN, representative of star-forming and active intermediate-redshift galaxies. These templates were computed for a half-dozen redshifts, and calibrated to have a flux of 22 μ Jy at 11 μ m. An illustrative plot of their spectral energy distribution (SED) is shown in Extended Data Fig. 2, in which the flux constraints at 1.6 and 870 μ m are also indicated by black symbols (square and triangle).

We used the rest-frame 8- μ m luminosity function of galaxies at redshifts between $z = 0.1$ and $z = 1$ in the Great Observatories Origins Deep Survey (GOODS) fields⁵⁰ to estimate the abundance of these star-forming galaxies. The 8- μ m luminosity was deduced from the templates. This led to a probability of 12% to find such a galaxy in the right redshift range ($z = 0.1$ to 1) in the 10×10 arcsec field of view. We estimated that there are about 80% star-forming galaxies and 20% active nuclei, including low-luminosity ones such as Seyfert galaxies^{51,52}. As can be seen in Extended Data Fig. 2, all templates comply with the three constraints below $z = 0.5$, and some starbursts are found brighter at 870 μ m above this redshift. We therefore reduced the probability accordingly for $z > 0.5$, attributing each star-forming template equal probability, as shown by the observations⁵³. The final probability to find such a galaxy in the 10×10 arcsec field of view is about 5%, with significant uncertainties: $+3/-2\%$. Hence, in a radius of 1.5 arcsec around TWA 7, the probability to have such a galaxy is about 0.34% ($+0.22/-0.14\%$). We note that the distribution of galaxies on the sky might be clustered in some rare places, and our error bars should be increased, but no more than 30% given the typical errors on luminosity function of galaxies^{45,47,50}. Altogether, the probability of having a galaxy satisfying the various constraints within 1.5 arcsec would be 0.34% ($+0.29/-0.18\%$). Note that the current calculation applies to these specific observational constraints. The probability for CC#1 to be a rare type of background galaxy compatible with the JWST, ALMA and SPHERE observational constraints is therefore low. Such a low-probability event can admittedly arise would a large number of independent datasets be analysed. However, this is not the case for this study. Indeed, only two datasets among about 30 JWST MIRI datasets dedicated to exoplanet searches

are analysed. Moreover, most of the other datasets are not as deep as the present ones, and there are no corresponding 1.6- and 870- μ m data available. Hence, the likelihood that any research group would have found such a peculiar background galaxy contaminant within the whole corpus of relevant JWST data is much lower than the simple 10.2% ($30 \times 0.34\%$) one could derive.

Data availability

All observational data in this work are available through public data archives. The JWST data were collected through General Observer programme number 3662 (principal investigator A.-M.L.) and will be available through the MAST database (<https://mast.stsci.edu>) from 21 June 2025. The data described here are available via the MAST archive at <https://doi.org/10.17909/4qvz-sw62>. The present study made use of ALMA data collected during the 2015.1.01015.S programme (principal investigator A. Bayo). The present study made use of detection limits derived from SPHERE data collected during the programme 198.C-0209, and of SPHERE data collected during the programmes 097.C-0319(A), 105.209E.001 and 198.C-0209(F). The data are available at <https://archive.eso.org>.

Code availability

JWST MIRI data reduction and analysis codes are available via GitHub at <https://github.com/mathildemalin/ExoCAT>. Data reduction was carried out using the publicly available JWST pipeline <https://jwst-pipeline.readthedocs.io/en/latest/>, and the stpf package <https://stpf.readthedocs.io/en/latest/> to simulate PSFs for JWST. We used various functions of the following software packages to perform the analysis and create the figures: numpy, astropy, scipy, matplotlib and photutils.

36. LaJoie, C.-P. et al. Small-grid dithers for the JWST coronagraphs. *SPIE Conf. Ser.* **9904**, 99045K (2016).
37. Boccaletti, A. et al. JWST/MIRI coronagraphic performances as measured on-sky. *Astron. Astrophys.* **667**, A165 (2022).
38. Málín, M. et al. Unveiling the HD 95086 system at mid-infrared wavelengths with JWST/MIRI. *Astron. Astrophys.* **690**, 316.
39. Boccaletti, A. et al. The four-quadrant phase mask coronagraph. IV. First light at the Very Large Telescope. *Astron. Astrophys.* **116**, 825 (2005).
40. Boccaletti, A. et al. The Mid-Infrared Instrument for the James Webb Space Telescope, V: predicted performance of the MIRI coronagraphs. *Publ. Astron. Soc. Pac.* **127**, 633 (2015).
41. Perrin, M. D. et al. Updated point spread function simulations for JWST with WebbPS. *Proc. SPIE* **9143**, 91433X (2014).
42. Nelder, J. A. & Mead, R. A simplex method for function minimization. *Comput. J.* **7**, 308–313 (1995).
43. Salo, H. et al. The Spitzer Survey of Stellar Structure in Galaxies (S4G): multi-component decomposition strategies and data release. *Astrophys. J. Supp. Ser.* **219**, 4 (2015).
44. Combes, F. Molecular gas in distant galaxies from ALMA studies. *Astron. Astrophys. Rev.* **26**, 5 (2018).
45. Ling, C.-T. et al. Galaxy source counts at 7.7, 10, and 15 μ m with the James Webb Space Telescope. *Mon. Not. R. Astron. Soc.* **517**, 85 (2022).
46. Wu, C. K. W. et al. Source counts at 7.7–21 μ m in CEERS field with JWST. *Mon. Not. R. Astron. Soc.* **523**, 5187–5197 (2023).
47. Stone, M. A. et al. 5–25 μ m galaxy number counts from deep JWST data. *Astrophys. J.* **972**, 62 (2024).
48. Sajkow, L. et al. Halfway to the peak: The JWST MIRI 5.6 μ m number counts and source population. *Astrophys. J.* **977**, 115 (2024).
49. Polletta, M. et al. Spectral energy distributions of hard X-ray selected active galactic nuclei in the XMM-Newton Medium Deep Survey. *Astrophys. J.* **663**, 81–102 (2007).
50. Caputi, K. et al. The infrared luminosity function of galaxies at redshifts $z=1$ and $z=2$ in the GOODS fields. *Astrophys. J.* **660**, 97 (2007).
51. Jarrett, T. H. et al. The Spitzer-WISE Survey of the ecliptic poles. *Astrophys. J.* **735**, 112 (2011).
52. Dale, D. et al. A two-parameter model for the infrared/submillimeter/radio spectral energy distributions of galaxies and active galactic nuclei. *Astrophys. J.* **784**, 83 (2014).
53. Bernard-Salas, J. et al. A Spitzer high-resolution mid-infrared spectral atlas of starburst galaxies. *Astrophys. J. Supp. Ser.* **184**, 230 (2009).

Acknowledgements This work is based on observations made with the JWST of NASA (National Aeronautics and Space Administration), the European Space Agency and the Canadian Space Agency. The data were obtained from the Mikulski Archive for Space Telescopes at the Space Telescope Science Institute, which is operated by the Association of Universities for Research in Astronomy, Inc., under NASA contract NAS 5-03127 for JWST. These observations are associated with programme number 3662. This paper makes use of ALMA data. ALMA is a partnership of the European Organisation for Astronomical Research in

the Southern Hemisphere (representing its member states), the National Science Foundation (USA) and the National Institutes of Natural Sciences (Japan), together with the National Research Council of Canada (Canada), the National Science Council and the Academia Sinica Institute of Astronomy and Astrophysics (Taiwan) and the Korea Astronomy and Space Science Institute (Republic of Korea), in cooperation with the Republic of Chile. The Joint ALMA Observatory is operated by the European Organisation for Astronomical Research in the Southern Hemisphere, the National Radio Astronomy Observatory operated by Associated Universities, Inc., and the National Astronomical Observatory of Japan. This paper makes use of observations collected at the European Organisation for Astronomical Research in the Southern Hemisphere. This project has received funding from the European Research Council under the European Union's Horizon 2020 research and innovation programme (COBREX; grant agreement number 885593). L.M. acknowledges funding by the European Union through the E-BEANS ERC project (grant number 100117693), and by the Irish Research Council under grant number IRCLA-2022-3788. Views and opinions expressed are those of the authors alone and do not necessarily reflect those of the European Union or the ERC Executive Agency. Neither the European Union nor the granting authority can be held responsible for them.

Author contributions A.-M.L. led the proposal, the interpretation of the various data and the writing of the paper. A. Boccaletti, M.M. and C.P. designed the JWST MIRI observing sequence, and reduced the data and participated in their interpretation. C.W. conducted the SED fitting. B.C. participated in the vetting of the Solar System origin of the source. A.R., B.C. and S.M. participated in discussions on the SED fitting. A. Chomez provided the SPHERE detection limit

maps used in this paper. A. Chomez, O.F., M.L., P.D. and G.C. participated in their interpretation. S.S. and T.B. tried to improve the detection limits using alternative algorithms. J. Milli participated in the building of the proposal, produced the SPHERE polarimetric images and participated the interpretation of the JWST MIRI data. A. Bayo and J.O. provided their analysis of the ALMA data, and participated in their interpretation. L.M. reanalysed the ALMA data and led the interpretation of these data. D.R. and F.C. conducted the estimation of the galaxy background probability. H.B. performed the *N*-body dynamical simulations. Q.K. and P.T. participated in the writing of the proposal and in the discussion of the disk–planet interactions. J. Mazoyer participated in the discussion of the disk properties. F.K. participated in the analysis of Gaia data, and general discussion. A. Carter and K.C. participated in the discussion on the astrometry of the source. P.R. participated in the proposal writing and the analysis of the data. All authors commented on the manuscript.

Competing interests The authors declare no competing interests.

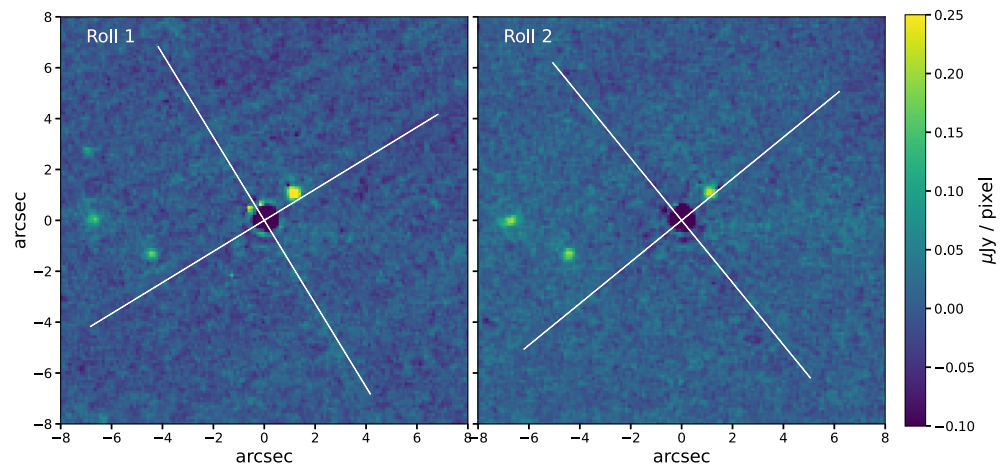
Additional information

Supplementary information The online version contains supplementary material available at <https://doi.org/10.1038/s41586-025-09150-4>.

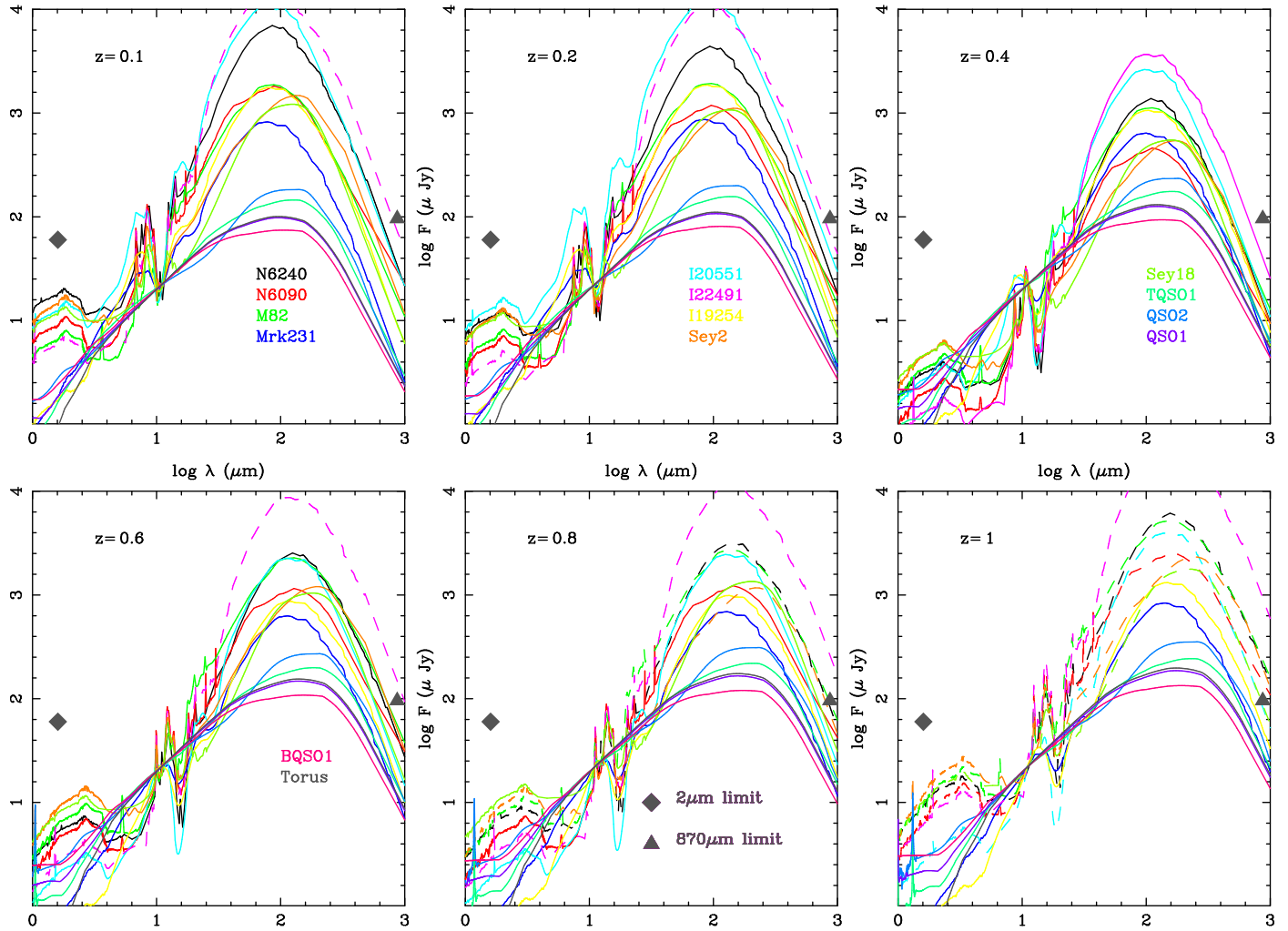
Correspondence and requests for materials should be addressed to A.-M. Lagrange.

Peer review information *Nature* thanks the anonymous reviewers for their contribution to the peer review of this work.

Reprints and permissions information is available at <http://www.nature.com/reprints>.

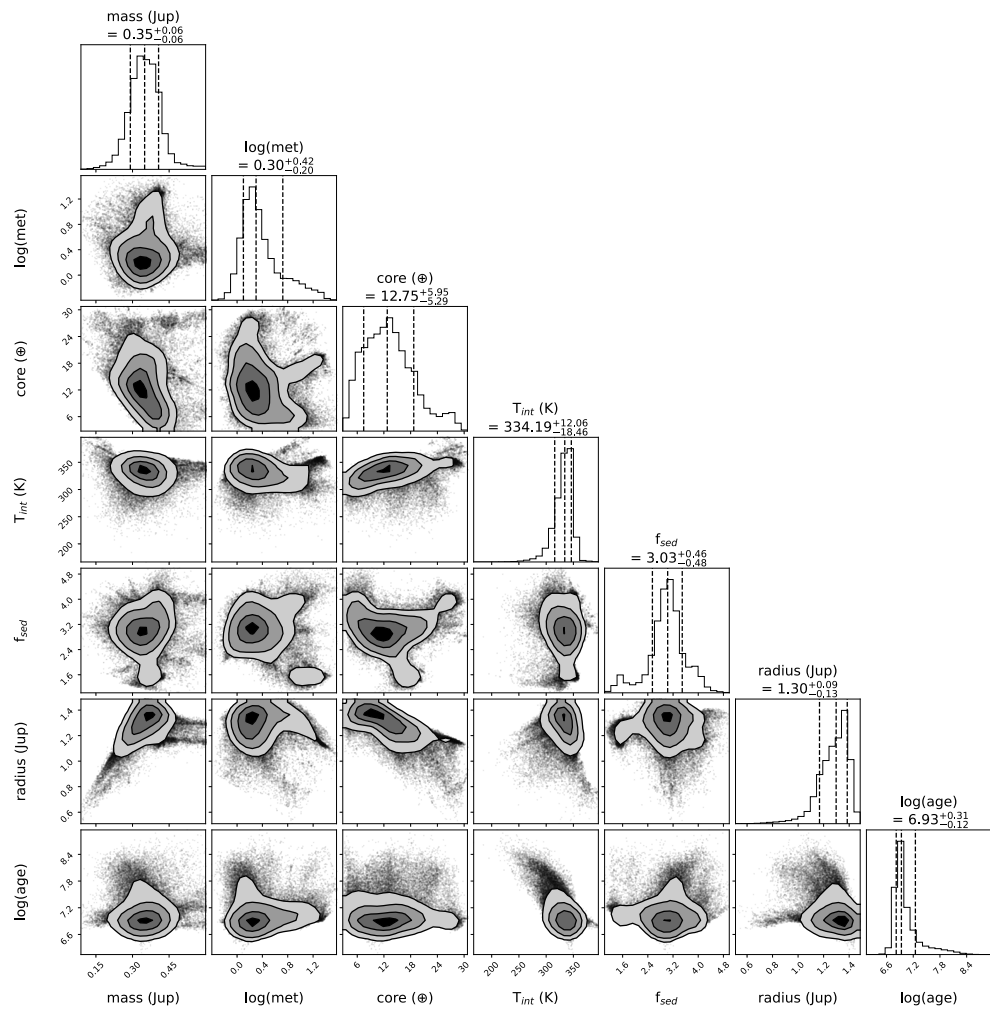


Extended Data Fig. 1 | JWST individual data sets. Orientation of the 4QPM and its phase transitions in the sky plane for the two telescope rolls. North is up, East is left.



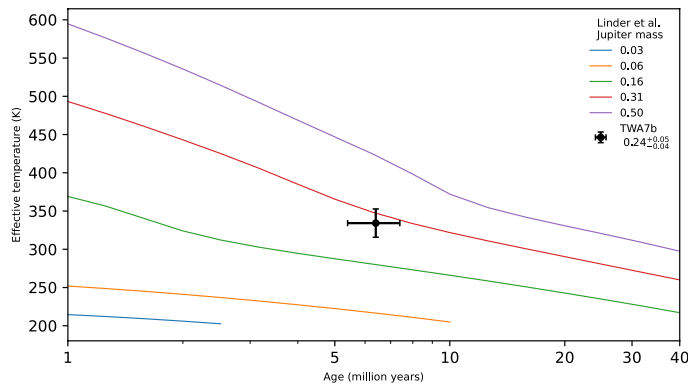
Extended Data Fig. 2 | SED of a set of 14 representative starburst galaxies and AGN at various redshifts. The curves are distinguished by their colors, and the corresponding labels, valid for all panels. All curves are calibrated to have a flux of 22 mJy at 11 μm. The two additional constraints are marked by

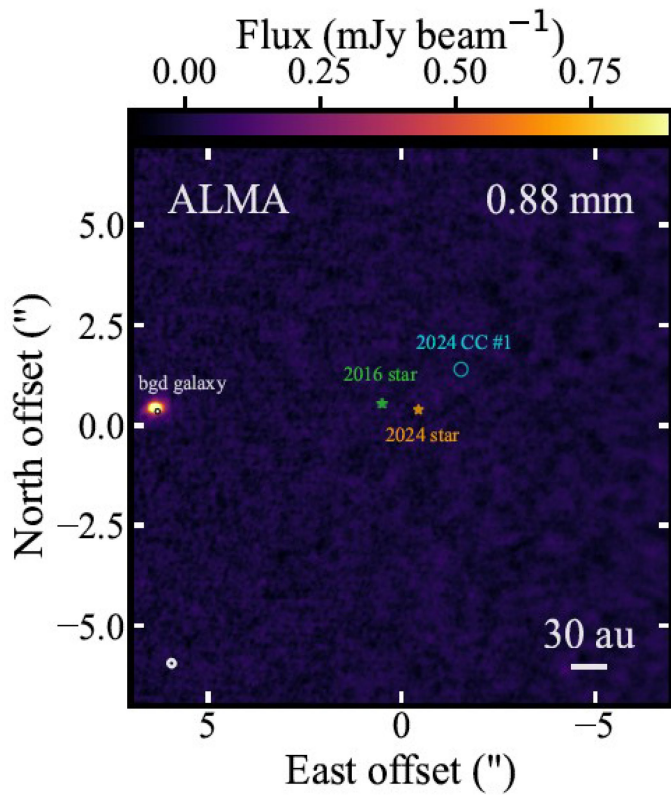
black symbols (square and triangle): the flux should be lower than 60 mJy at 1.6 μm, and 96 mJy at 870 μm. The SED which are not consistent with the limits are plotted in dashed lines.



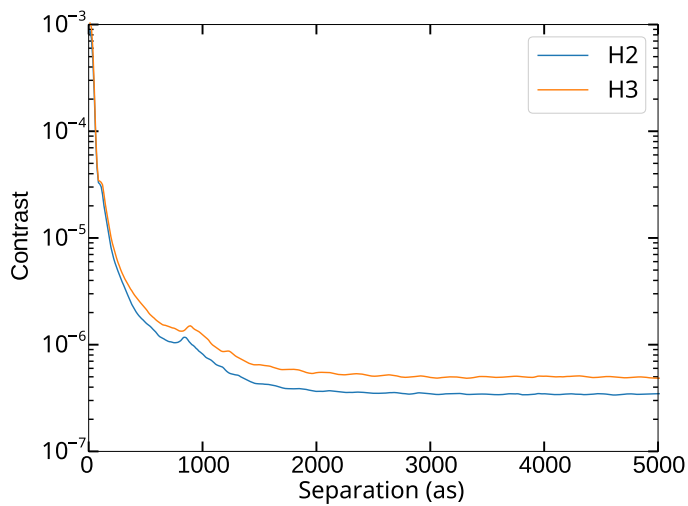
Extended Data Fig. 3 | Planet characterization. Corner plot of cloudy forward modeling using SPHERE upper limits and age constraints of 6.4 ± 1 Myr. The associated priors are listed in Extended Data Table 3. The mass found is

$0.34 \pm 0.06 M_J$ (considering errors from the MCMC only). Core given in Earth mass, T_{int} corresponds to the intrinsic temperature and f_{sed} the sedimentation rate of the considered clouds.





Extended Data Fig. 5 | ALMA image of TWA7. Combined ALMA 0.88 mm image of the TWA 7 system obtained with Briggs 0.5 weighting, centered at the phase center of the April compact configuration observations. The background galaxy is clearly detected East of the expected stellar position, at a position consistent with the East source detected by MIRI (black and white circle). The stellar location at each of the 2016 ALMA epochs is shown by the green star (positions largely overlapping), whereas the stellar location at the 2024 MIRI observation is shown by the orange star. The position of the CC#1 source at the epoch of the 2024 MIRI observation is shown by the cyan circle. The image (not primary beam-corrected) has a resolution of $0.19'' \times 0.18''$ (shown as the circle in the bottom left of the image) and an RMS noise level of $23 \mu\text{Jy/beam}$.



Extended Data Fig. 6 | SPHERE detection limits. Contrast 5-sigma confidence level curves of the SPHERE observation used to compute the upper limits on the candidate companion flux.

Article

Extended Data Table 1 | Log of observations

Target name	Filter	Set up	Read-out	Groups/Int	Int./exp	Exposures/Dit	Dither	Total exposure time (s)	N roll
TWA7 (Science)	F1140C	4QPM_1140	FASTR1	500	60	1	1	7204	2
CD-23-9765 (Reference)	F1140C	4QPM_1140	FASTR1	300	6	1	9	3894	1
Background TWA7	F1140C	4QPM_1140	FASTR1	500	60	1	2	7204	1
Background Reference	F1140C	4QPM_1140	FASTR1	300	6	1	2	865	1

Extended Data Table 2 | Astrometry and photometry of sources detected within 10" from TWA 7

Source	Delta RA (arcsec)	Delta Dec (arcsec)	Flux (W/m ² /um)	Resolved?
CC#1	-1.10±.03	1.01±0.03	5.60±0.97 e-19	No
Star BKG	4.49±0.01	-1.37±0.01	1.52±0.36 e-19	No
Gal BKG	6.74±0.04	-0.05±0.04	1.76±0.55 e-19	Yes

Article

Extended Data Table 3 | Uniform priors used in forward modeling approach

	Mass (M_{Jup})	Metallicity [Fe/H]	Core mass (M_{Earth})	Effective temperature (K)	Cloud sedimentation rate
Uniform priors	[0.01,2]	[-2,1.6]	[1,40]	[1,2000]	[1,5]